DISCRETE AND CONTINUOUS
DYNAMICAL SYSTEMS–SERIES B
Volume **xx**, Number **0xx**, xx **2006**

Website: http://AIMsciences.org

pp. **xx-xx**

MULTIRESOLUTION ANALYSIS FOR 2D TURBULENCE. PART 2: A PHYSICAL INTERPRETATION

CH.-H. BRUNEAU, P. FISCHER, H. KELLAY

University Bordeaux 1
33405 Talence Cedex, France

Abstract. Multiresolution methods like the wavelet packets or the cosine packets are more and more used in physical applications and in particular in two-dimensional turbulence. The theoretical bases of these decompositions have been introduced in the first part of this paper. The numerical results have shown that the wavelet packets decomposition is well suited for studying this kind of problem: the visualization of the vorticity field is better, without any kind of artifacts contrary to the visualization with the cosine packets filtering. The current second part of the paper is devoted to the physical interpretation of the filtering process proposed in the first part. Only the wavelet packets decomposition is considered here since the cosine packets did not give an entire satisfaction.

1. **Introduction.** We have shown in the first part of this paper [6] that the wavelet packets filtering can be successfully used for analyzing two-dimensional turbulence. This technique allows to separate two kinds of structures, the solid rotations composed by the core of the vortices from the background mainly composed by vorticity filaments. Furthermore, contrary to a direct cut-off filtering, the wavelet packets filtering leads to continuous filtered fields. The spurious effects of the discontinuities created by a direct filtering have been discussed in [7]. There, it was shown that the discontinuities are responsible for the creation of spurious coefficients in Fourier space thus altering the corresponding energy and enstrophy spectra.
The goal of this second part is to refine the explanations given in the first part and to detail the physical interpretation of the filtered fields given in [4]. In particular, the energy and enstrophy fluxes have been computed and allow to get a better understanding of the energy and enstrophy transfer processes through the scales. A few results about the pressure field are also given in the paper.

2. **Theoretical background.** Two dimensional turbulence, in a finite but periodic domain, is governed by two invariants, the energy and the enstrophy. The mean energy *per unit mass* E is defined by,

$$E \equiv \left\langle \frac{1}{2}|\boldsymbol{v}|^2 \right\rangle = \frac{1}{2}\frac{1}{S(B_L)}\int_{B_L} |\boldsymbol{v}(\boldsymbol{x})|^2 d\boldsymbol{x} \tag{1}$$

where B_L denotes the physical domain of definition of $\boldsymbol{v}$ and $S(B_L)$ its corresponding surface. If one considers now $\boldsymbol{v}$ as a L-periodic function, it can be decomposed

2000 *Mathematics Subject Classification.* 65T60,76F65.
Key words and phrases. Wavelets, 2D turbulence.

as a Fourier series:

$$\boldsymbol{v}(\boldsymbol{x}) = \sum_{\boldsymbol{k}} \hat{\boldsymbol{v}}(\boldsymbol{k}) e^{\frac{2i\pi}{L}\boldsymbol{k}.\boldsymbol{x}}, \quad \boldsymbol{k} \in \mathbb{Z}^2. \tag{2}$$

The low-pass filtered velocity function is then defined as,

$$\boldsymbol{v}_K^<(\boldsymbol{x}) = \sum_{|\boldsymbol{k}|\leq K} \hat{\boldsymbol{v}}(\boldsymbol{k}) e^{\frac{2i\pi}{L}\boldsymbol{k}.\boldsymbol{x}} \tag{3}$$

and the high-pass filtered velocity function as:

$$\boldsymbol{v}_K^>(\boldsymbol{x}) = \sum_{|\boldsymbol{k}|> K} \hat{\boldsymbol{v}}(\boldsymbol{k}) e^{\frac{2i\pi}{L}\boldsymbol{k}.\boldsymbol{x}}. \tag{4}$$

This decomposition of the velocity,

$$\boldsymbol{v}(\boldsymbol{x}) = \boldsymbol{v}_K^<(\boldsymbol{x}) + \boldsymbol{v}_K^>(\boldsymbol{x}), \tag{5}$$

was used for the first time by Obukhov [12], [13]. Introducing this splitting in the Navier-Stokes equations, one obtain a scale-by-scale energy budget equation described by Frisch [8]:

$$\partial_t \mathcal{E}(K) + \Pi_E(K) = \mathcal{D}_E(K) + \mathcal{F}_E(K). \tag{6}$$

where

$$\mathcal{E}(K) \equiv \left\langle \frac{1}{2}|\boldsymbol{v}_K^<|^2 \right\rangle = \frac{1}{2}\sum_{|\boldsymbol{k}|\leq K} |\hat{\boldsymbol{v}}(\boldsymbol{k})|^2, \tag{7}$$

denotes the cumulative energy, $\Pi_E(K)$ the energy flux due to the non linear terms through the wavenumber K, $\mathcal{D}_E(K)$ the energy dissipation, and $\mathcal{F}_E(K)$ the energy injection. The energy spectrum is then defined by,

$$E(k) \equiv \frac{d\mathcal{E}(k)}{dk}, \tag{8}$$

and the total energy can be rewritten as,

$$E = \int_0^\infty E(k)dk. \tag{9}$$

The same splitting can be used in the Navier-Stokes equation written for the vorticity and a scale-by-scale enstrophy budget equation can be obtained:

$$\partial_t \mathcal{Z}(K) + \Pi_Z(K) = \mathcal{D}_Z(K) + \mathcal{F}_Z(K), \tag{10}$$

where $\mathcal{Z}(K)$ denotes the cumulative enstrophy, $\Pi_Z(K)$ the enstrophy flux, $\mathcal{D}_Z(K)$ the enstrophy dissipation, and $\mathcal{F}_Z(K)$ the enstrophy injection. The enstrophy Z can be defined in the same way as the energy,

$$Z \equiv \left\langle \frac{1}{2}|\omega|^2 \right\rangle = \frac{1}{2}\frac{1}{S(B_L)}\int_{B_L} |\omega(\boldsymbol{x})|^2 d\boldsymbol{x}, \tag{11}$$

where $\omega = \boldsymbol{\nabla} \times \boldsymbol{v}$ is the vorticity field. The relation between the enstrophy and the enstrophy spectrum is then given by:

$$Z = \int_0^\infty Z(k)dk \tag{12}$$

where $Z(k)$ stands for the enstrophy spectrum. The energy and enstrophy spectra are linked to each other in Fourier space by the following relation:

$$Z(k) = \left(\frac{2\pi k}{L}\right)^2 E(k) \tag{13}$$

which reduces to

$$Z(k) = k^2 E(k) \tag{14}$$

in a 2π-periodic bounded domain. Using the same notation as Tung and Gkioulekas in [16] this relation can be written in a more general form:

$$Z(k) = \Lambda(k) E(k). \tag{15}$$

The fluxes are also related to each other by the same kind of relation:

$$\frac{\partial \Pi_Z(k)}{\partial k} = \Lambda(k) \frac{\partial \Pi_E(k)}{\partial k}. \tag{16}$$

Outside the forcing range, the fluxes should verify the following inequality:

$$\Lambda(k)\Pi_E(k) < \Pi_Z(k). \tag{17}$$

This inequality is a consequence of the classical boundary conditions: periodic or infinite. However, as described in [6], our experiments consist in the numerical simulation of two-dimensional channel flow perturbed by arrays of cylinders with a no-slip boundary condition in the across-channel direction. A non homogeneous Dirichlet condition is imposed in the beginning of the channel, and an absorbing condition is imposed at the end. The spectra are computed in a selected square located at the end of the channel. Thus we do not have any periodic condition in any case, and the relations described above between the energy and the enstrophy spectra do not hold anymore. It has been shown in [7] that the energy-enstrophy relation numerically diverges in our particular case. A detailed study has been performed, and the results have shown that a Windowed Fourier Transform has to be used for the spectra computations in order to remove the discontinuities created by the boundary conditions.

3. **The experimental setup and the filtering process.**

3.1. **Experimental setup.** In the first part [6], two numerical experiments, called *simulation I* and *II*, had been performed. Slightly different versions of *simulation II* are considered in this paper. The additional cylinders along the channel are still useful in order to increase the number of merging events, and thus to enhance the inverse energy cascade phenomenon. In the first part, the energy injection scale k_{inj} had been considered to be equal to the diameter of the five big cylinders ($k_{inj} \approx 10$). But it is a matter of fact that the small cylinders along the sides of the channel induce a second small energy injection around $k = 20$. So the energy injection should be considered to lie between 10 and 20. In order to get a better localized energy injection, the five big cylinders have been replaced by ten small cylinders. From now, all the obstacles have the same diameter and induce the same energy injection scale. The Reynolds number based on the cylinders diameter is $Re = 50000$ that is large enough to get a fully developed turbulent flow. This is about the same value as those used in soap film experiments [5, 11]. A snapshot of the vorticity field is given in Figure 1

The simulations have been performed on a 640×2560 grid and the averages have been computed with 25 snapshots. A Tukey window with the parameter equal to 0.1 has been used in all the computations in order to remove the discontinuities created by the boundary conditions.

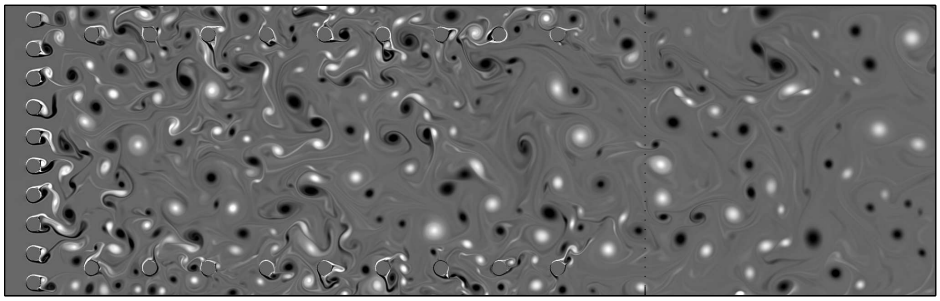

FIGURE 1. Snapshot of the vorticity field

3.2. **The filtering process.** The theory concerning the wavelet packets has been already detailed in [6] and will not be reminded here. The same Daubechies type wavelets are used in the current paper to build the packets array, and the entropy criterion is used in the best basis selection process. In [6], few tests had been performed in order to get the best wavelet mother, and to determine the number of scales necessary for an efficient representation of the flow. The criterion was then the minimization of the entropy. It had been shown that it was not necessary to perform the wavelet packets decomposition over more than 3 scales when the finest scale corresponds to a 320×1280 grid. It has to be reminded that the scale sequence goes from finest scales to coarsest scales. It leads to the most efficient representation in the *entropy* meaning but not to the smoothest fields after filtering. It has been shown in [7] that, as long as one is concerned with smoothing the discontinuities, it is necessary to go over at least 4 scales (for a finest scale corresponding to a 320×1280 grid). That means that in [6], where only 3 scales were considered, some spurious coefficients due to the discontinuities remained in the spectra, and the slopes detected in the figures were partly altered. So in the results presented in this second part of the paper, all the decompositions have been performed over 5 scales for a 640×2560 grid. The overall filtering process can be summarized as follows:

1. Computation of the wavelet packets decomposition of the two components of the velocity $\boldsymbol{v} = (u, v)$ over 5 scales.
2. Separation of the velocity fields into two subfields: one subfield, $\boldsymbol{v_s} = (u_s, v_s)$, where the wavelet packet coefficients have their modulus larger than a given threshold ϵ and another one, $\boldsymbol{v}_f = (u_f, v_f)$ where the wavelet packet coefficients are smaller than ϵ.
3. Construction of the corresponding vorticity fields, ω_s and ω_f. The filtered field ω_s is then essentially composed by solid rotations, and the ω_f by vorticity filaments.
4. Computations of the physical data: energy/enstrophy spectra/fluxes.

The velocity decomposition $\boldsymbol{v} = \boldsymbol{v_s} + \boldsymbol{v_f}$ is orthogonal and leads to the energy spectrum decomposition:

$$E(k) = E_s(k) + E_f(k), \tag{18}$$

as can be verified in Figure 2.

First of all, we have to remark that because of the use of the windowing the slopes in the original spectrum are steeper than the ones shown in [6]. Now we

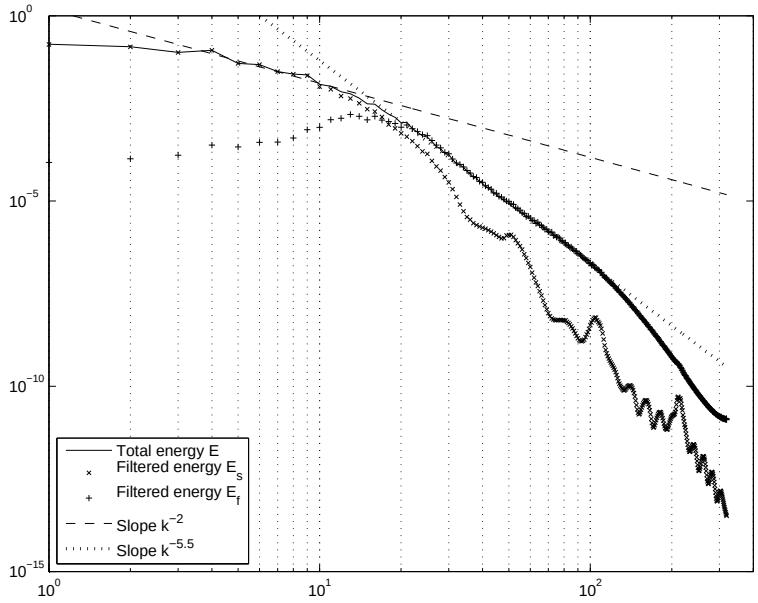

FIGURE 2. Original and filtered (WP 5 scales) energy spectra ($k_{inj} \approx 20$).

observe a first slope around k^{-2} and a second slope around $k^{-5.5}$. This is due to the fact that all the spurious coefficients due to the discontinuities have been removed. One can then notice that both components are multiscale, although the part with the vortices dominates at low wavenumbers and the part mainly composed by filaments dominates at high wavenumbers. The first slope is not really clear but the second one is evident. These slopes and this decomposition can be also observed on the enstrophy spectra given in Figure 3. It has been shown in [7] that the relation (15) with $\Lambda(k) = 4\pi^2 k^2$ between the energy and the enstrophy spectra is verified only in the middle part of the spectra.

Remark: The pressure field is rarely studied in papers about two-dimensional turbulence but nevertheless can bring interesting information about the fluid. A snapshot of the end of the pressure field is given in Figure 4.

The pressure field can be compared to the corresponding vorticity field. The decomposition into the two subfields obtained by the filtering process is also given in Figure 4.

As can be easily observed, the peaks of the pressure correspond exactly to vorticity peaks. They correspond obviously to the solid rotation structures, and it can be expected that the pressure spectrum should present the same behavior as the solid rotations spectrum. Both spectra are given in Figure 6 and the similarity between the shape of the pressure spectrum and the shape of the solid rotations energy spectrum is clear.

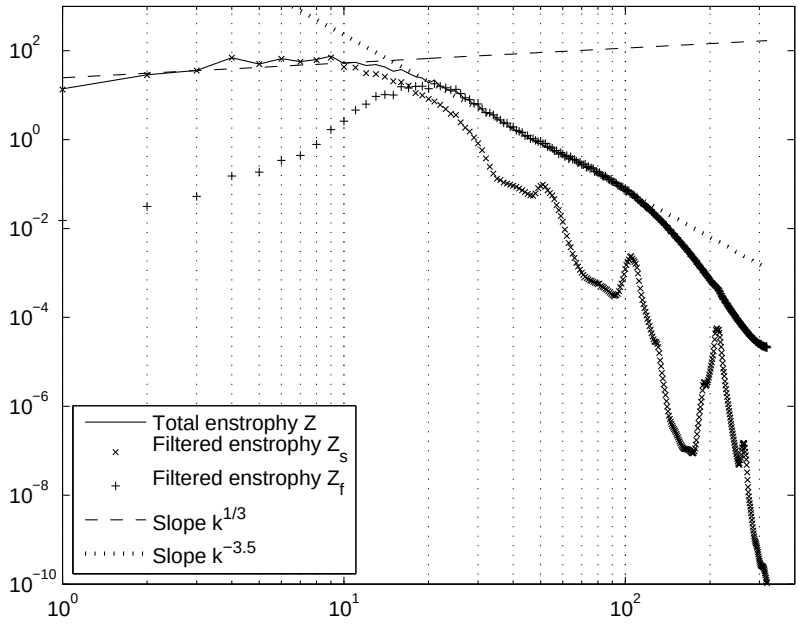

FIGURE 3. Original and filtered (WP 5 scales) enstrophy spectra ($k_{inj} \approx 20$).

4. **Energy and enstrophy fluxes.** We recall that the energy flux is computed from the non linear term in the Navier-Stokes equation written in Fourier space:

$$\Pi_E(k) = \int_k^{+\infty} T_E(k')dk' \tag{19}$$

where $T_E(k)$ is the nonlinear energy transfer function and is obtained by angular integration of $\widehat{\boldsymbol{v}^*(\boldsymbol{k})}.\widehat{(\boldsymbol{v}.\nabla)\boldsymbol{v}(\boldsymbol{k})}$. The enstrophy flux is obtained in the same way:

$$\Pi_Z(k) = \int_k^{+\infty} T_Z(k')dk' \tag{20}$$

where $T_Z(k)$ is the enstrophy transfer function and is obtained by angular integration of $\widehat{w^*(\boldsymbol{k})}.\widehat{(\boldsymbol{v}.\nabla)w(\boldsymbol{k})}$.

The inequality in equation (17) brought to the attention of Tung and Gkioulekas by Danilov has been discussed in [16]. According to Tung and Gkioulekas, if an inertial range exists, then this inequality describes the process of the transition from the leading cascade to the subleading cascade observed in the energy spectrum. As can be noticed in Figure 7, this inequality is verified almost everywhere except in a small range at large scales. It is not surprising since the inertial range does not stretch out on large scales. It has been mentionned by Tran in [15] that the behavior at large scales of a fluid in an elongated and doubly periodic domain is far from understood. He describes in that paper how the inverse energy cascade can be partially stopped. Furthermore in our case, the boundary conditions are different

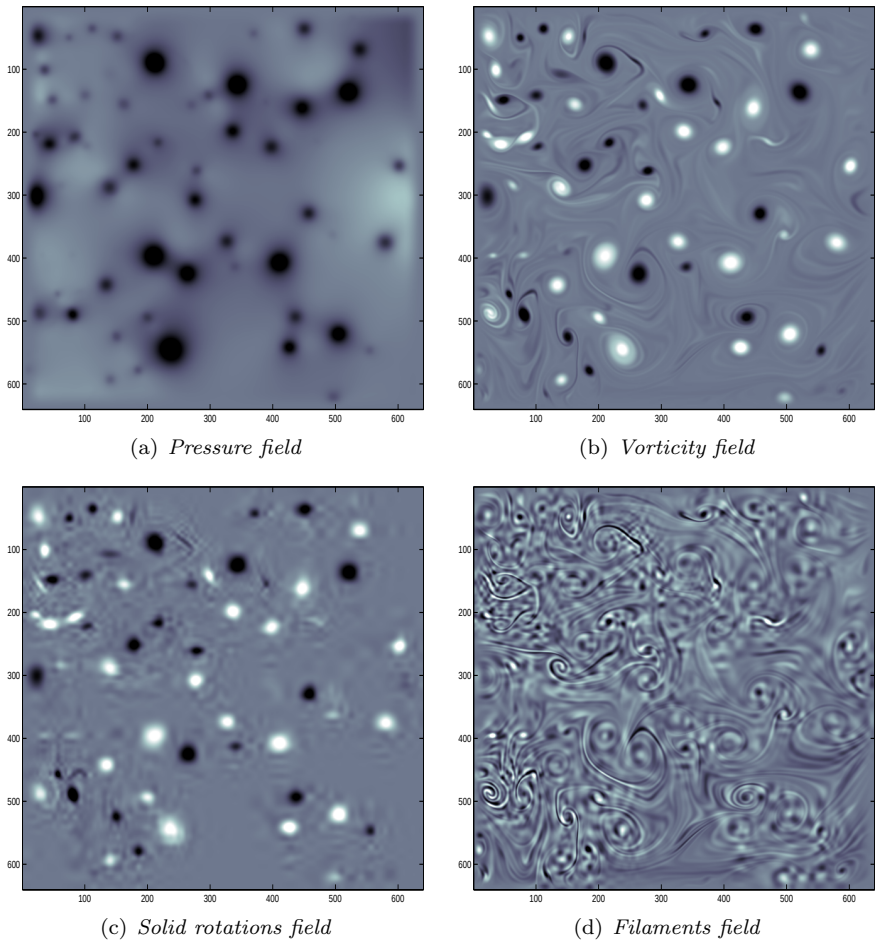

(a) *Pressure field* (b) *Vorticity field*

(c) *Solid rotations field* (d) *Filaments field*

FIGURE 4. Snapshots at the end of the channel ($k_{inj} \approx 20$)

and the fluid dynamics at large scale is very hard to predict. However, it can be noticed that the inequality is verified around $k = 20$ which is supposed to be the injection scale.

Let us now study the energy and enstrophy fluxes themselves. The energy and enstrophy fluxes corresponding to those experiments are respectively given in Figure 8 and 9. The energy flux is negative for wavenumbers k below the injection scale 20 and slightly positive above. The enstrophy flux is on the other hand positive above the injection scale, and negative below. The zero crossing corresponds approximately to the injection scale. These results show the existence of leading cascades, upscales for the inverse energy cascade and downscales for the direct enstrophy cascade but also the existence of subleading cascades as theoretically shown by Tung and Gkioulekas in [9, 10] and [16]. It can also be noticed that the injection scale being relatively large, the energy cascade cannot be developed completely. On the other side, the enstrophy cascade does not present any "plateau" because we did not use any artificial dissipation term like an hyperviscosity term. The two

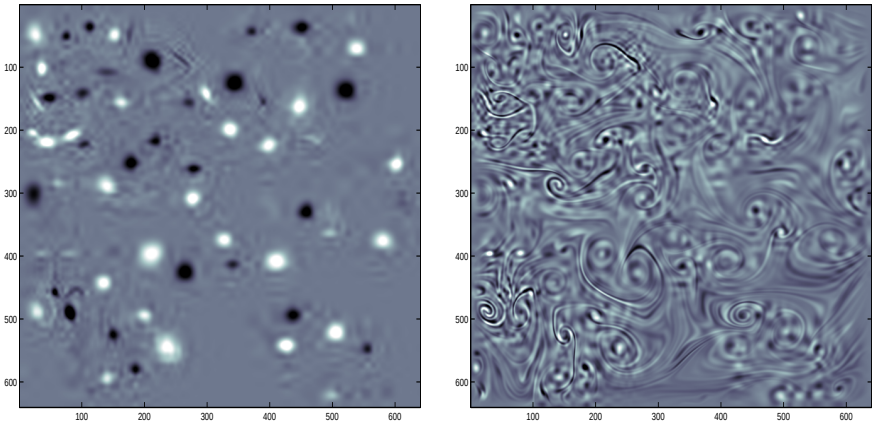

(a) *Solid rotations field* (b) *Filaments field*

FIGURE 5. Snapshots at the end of the channel ($k_{inj} \approx 20$)

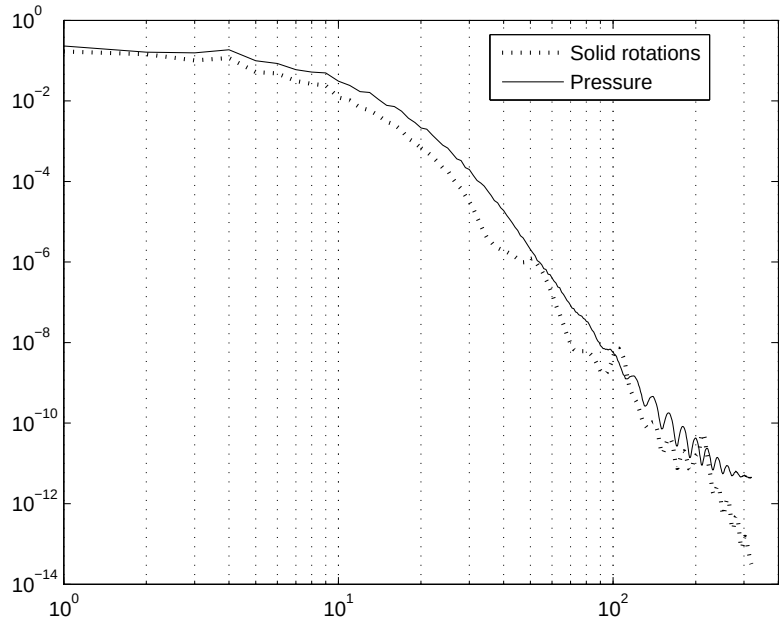

FIGURE 6. Pressure and solid rotations spectra ($k_{inj} \approx 20$).

cascades could be improved by using artificial dissipation terms at large and small scales.

4.1. **Fluxes for the filtered fields.** In order to study, in detail, the energy transfer, we focus now on the nonlinear energy transfer function which, due to the

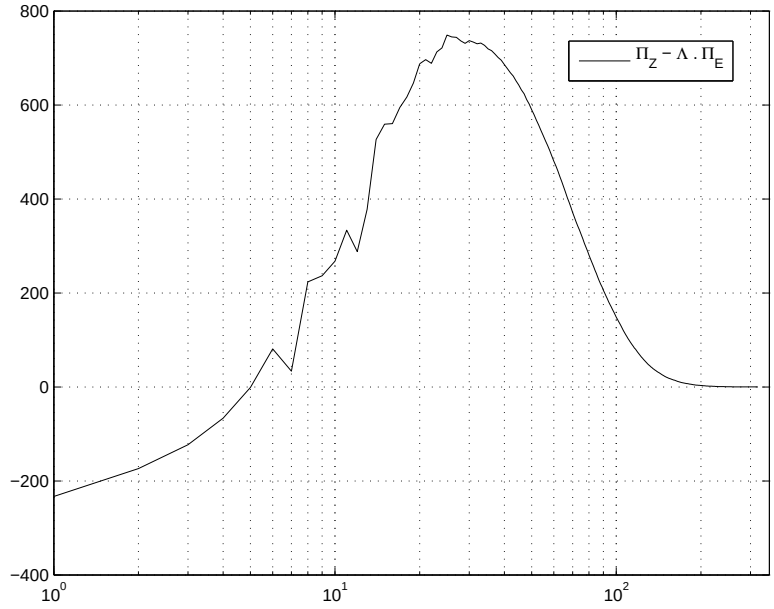

FIGURE 7. $\Pi_Z - \Lambda\Pi_E$ allowing to verify the Danilov inequality.

orthogonal decomposition, can be written as:

$$\begin{aligned} T_E(\boldsymbol{k}) &= \widehat{\boldsymbol{v}^*(\boldsymbol{k})}.\widehat{(\boldsymbol{v}.\nabla)\boldsymbol{v}}(\boldsymbol{k}) \\ &= \widehat{\boldsymbol{v_s}^*(\boldsymbol{k})}.\widehat{(\boldsymbol{v}.\nabla)\boldsymbol{v_s}}(\boldsymbol{k}) \;+\; \widehat{\boldsymbol{v_s}^*(\boldsymbol{k})}.\widehat{(\boldsymbol{v}.\nabla)\boldsymbol{v_f}}(\boldsymbol{k}) \\ &\quad + \widehat{\boldsymbol{v_f}^*(\boldsymbol{k})}.\widehat{(\boldsymbol{v}.\nabla)\boldsymbol{v_s}}(\boldsymbol{k}) \;+\; \widehat{\boldsymbol{v_f}^*(\boldsymbol{k})}.\widehat{(\boldsymbol{v}.\nabla)\boldsymbol{v_f}}(\boldsymbol{k}). \end{aligned} \tag{21}$$

The global energy transfer can be split into four parts corresponding to the multiscale transfers from one subfield to itself or to the other one. For instance, $\widehat{\boldsymbol{v_s}^*}(\boldsymbol{k}).\widehat{(\boldsymbol{v}.\nabla)\boldsymbol{v_f}}(\boldsymbol{k})$ is the energy transfer from the vorticity filaments subfield to the solid rotation subfield. The fluxes corresponding to each term in the expression for the total energy transfer function will be denoted as for example $\Pi_E^{f\to s}$ which is the flux corresponding to the transfer term previously described. In the same way, the nonlinear enstrophy transfer term is also split into four parts:

$$\begin{aligned} T_Z(\boldsymbol{k}) &= \widehat{\omega^*(\boldsymbol{k})}.\widehat{(\boldsymbol{v}.\nabla)\omega}(\boldsymbol{k}) \\ &= \widehat{\omega_s^*(\boldsymbol{k})}.\widehat{(\boldsymbol{v}.\nabla)\omega_s}(\boldsymbol{k}) \;+\; \widehat{\omega_s^*(\boldsymbol{k})}.\widehat{(\boldsymbol{v}.\nabla)\omega_f}(\boldsymbol{k}) \\ &\quad + \widehat{\omega_f^*(\boldsymbol{k})}.\widehat{(\boldsymbol{v}.\nabla)\omega_s}(\boldsymbol{k}) \;+\; \widehat{\omega_f^*(\boldsymbol{k})}.\widehat{(\boldsymbol{v}.\nabla)\omega_f}(\boldsymbol{k}). \end{aligned} \tag{22}$$

Using these decompositions, the fluxes associated with each structure as well as the fluxes associated with the interactions of the two structures can be obtained. Let us first consider the energy fluxes of the whole flow and of the separate structures in Figure 8.

The energy flux for the vortices shows a large negative part at small k which is similar to the total flux and becomes very small and close to zero beyond the

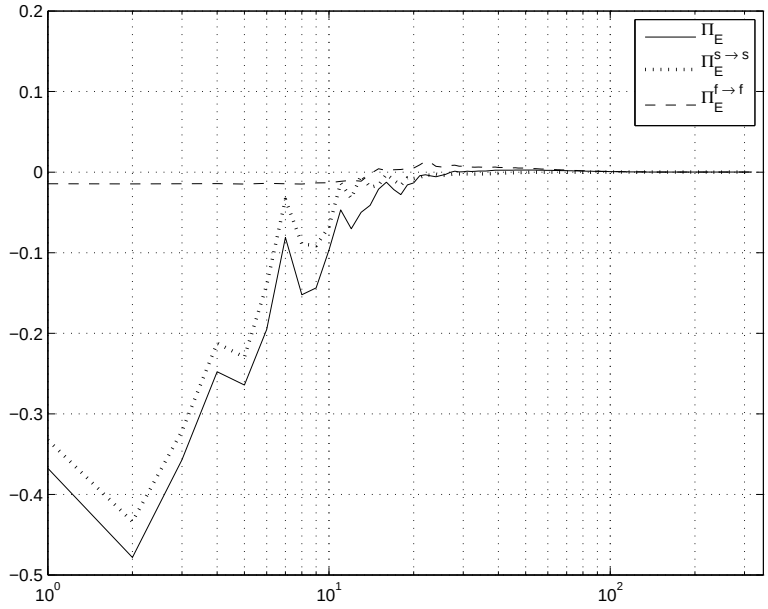

FIGURE 8. Energy fluxes of the whole flow and of the separate structures ($k_{inj} \approx 20$).

injection scale. The energy flux associated with the filaments is negative but small at small k and becomes slightly positive near the injection scale before becoming zero at the high k end.

The enstrophy flux for the vortices is negative at small k and becomes close to zero beyond the injection scale. The enstrophy flux for the filaments is on the other hand large and positive for the high k after the injection scale and is very close to the value of the total flux in this region of wavenumbers. This preliminary examination of the fluxes indicates that the main part of the energy flux comes from the solid rotations while the main part of the enstrophy flux comes from the filamentary structures.

It is however possible to give a more detailed analysis of the energy and enstrophy transfers. When computing the nonlinear terms, we are comparing in fact the Fourier spectrum of a two dimensional field, $\widehat{\omega_s(\boldsymbol{k})}$ for instance, to the Fourier spectrum of a transported field, $(\boldsymbol{v}.\widehat{\nabla)\omega_f}(\boldsymbol{k})$ on the other hand. The energy flux from the vortices to the filaments and vice versa are an order of magnitude smaller than the flux due to the filaments or the flux due to the vortices. However, the cross fluxes of enstrophy show an interesting feature in Figure 10. $\Pi_Z^{f\to s}$ and $\Pi_Z^{s\to f}$ are of opposite sign and have amplitudes comparable to the total enstrophy flux. However, the sum of these two fluxes $\Pi_Z^{f\to s} + \Pi_Z^{s\to f}$ turns out to be very close to zero. While the transfer from the filaments to the vortices is positive at small k and very close to zero beyond the injection scale, the flux of enstrophy from the vortices to the filaments is negative at small k and goes to zero at high k. Although both fluxes compensate each other, there is a clear interaction between the two different

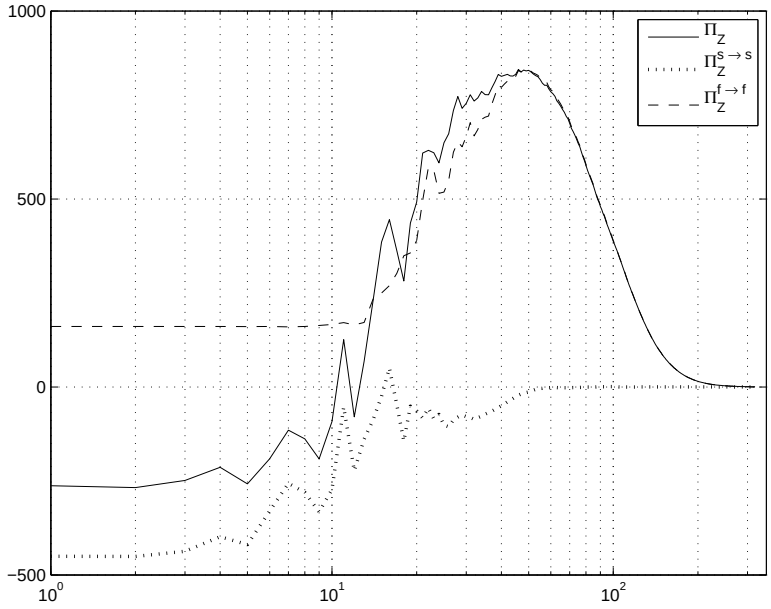

FIGURE 9. Enstrophy fluxes of the whole flow and of the separate structures ($k_{inj} \approx 20$).

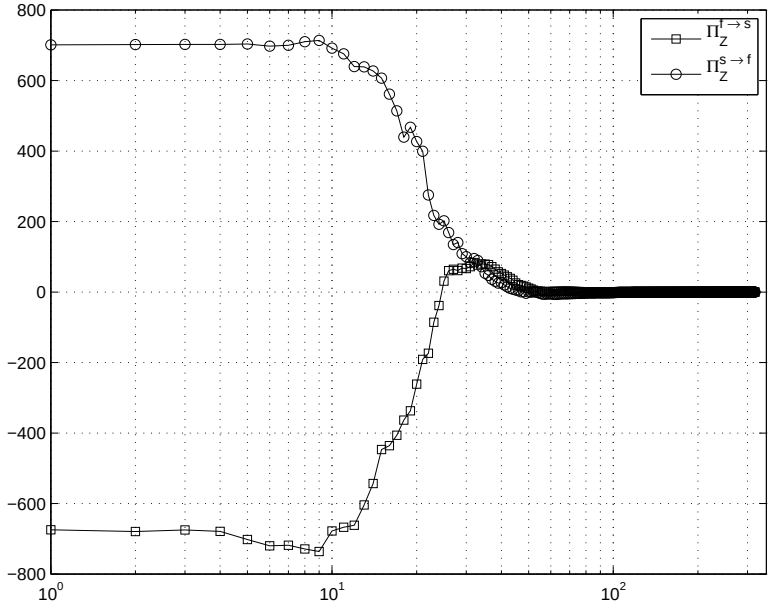

FIGURE 10. Cross fluxes of enstrophy ($k_{inj} \approx 20$).

structures. The vortices transfer enstrophy to the filaments from the small scales to the large scales while the filaments transfer enstrophy to the vortices from large scales to the small scales.

4.2. **The inverse energy cascade.** In order to improve the generation of each cascade separately, one can try to move the injection scale from one side of the spectrum to the other one. However, the possible shifts are very limited due to numerical constraints. The penalization method used to take into account the obstacles in the equations and the discretization step size do not allow the use of very small cylinders. One can however define obstacles of size corresponding to an injection scale of $k_{inj} \approx 40$. The Reynolds number is still kept equal to 50000 in these new numerical computations. The computations have been performed on a grid of size 1024×4096. A snapshot corresponding to this new geometry is given in Figure 11. The statistics to compute the fluxes have been performed only on 20 snapshots in order to limit the size of the data. Consequently the fluxes are less smooth than in the previous case.

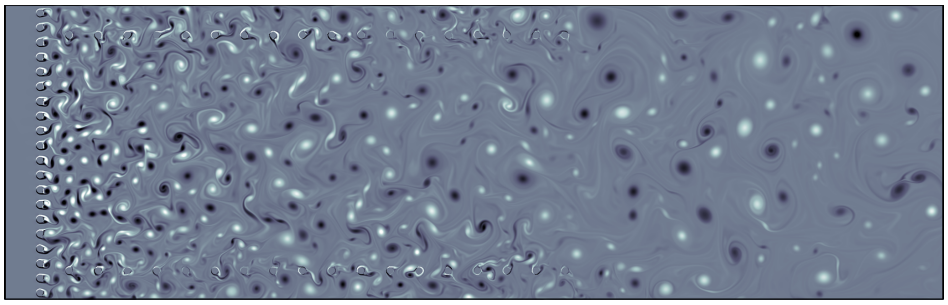

FIGURE 11. Snapshot of the vorticity field

As can be expected, the inverse energy cascade has more room to take place and the energy flux tends to go to zero at the largest scales (Figure 12) and goes back to zero close to the injection scale ($k \approx 40$).
The direct enstrophy cascade still exists at scales larger than the injection scale (Figure 13) and can be observed until $k \approx 100$. One can also notice that the enstrophy flux crosses the zero axis around the injection scale ($k \approx 40$).

4.3. **The direct enstrophy cascade.** In order to study the direct enstrophy cascade, the geometry of the numerical experiment has been modified again. The turbulence is now created by three arrays of big cylinders.This setup produces an injection scale k_{inj} located around $k = 9$ ($Re = 50000$). The computations have been performed on a grid of size 512×2048. A snapshot of the vorticity field corresponding to this setup is given in Figure 14.

As can be verified on the corresponding energy flux given in figure 15, the injection scale is too large to allow the development of a full inverse energy cascade.

The enstrophy flux is given in Figure 16 and it can be observed on the graph that the direct enstrophy cascade beyond the injection scale does exist. But it can also be observed a strong enstrophy transfer from the injection scale toward the largest scales. One notice again that the enstrophy flux crosses the zero axis around the injection scale ($k \approx 9$).

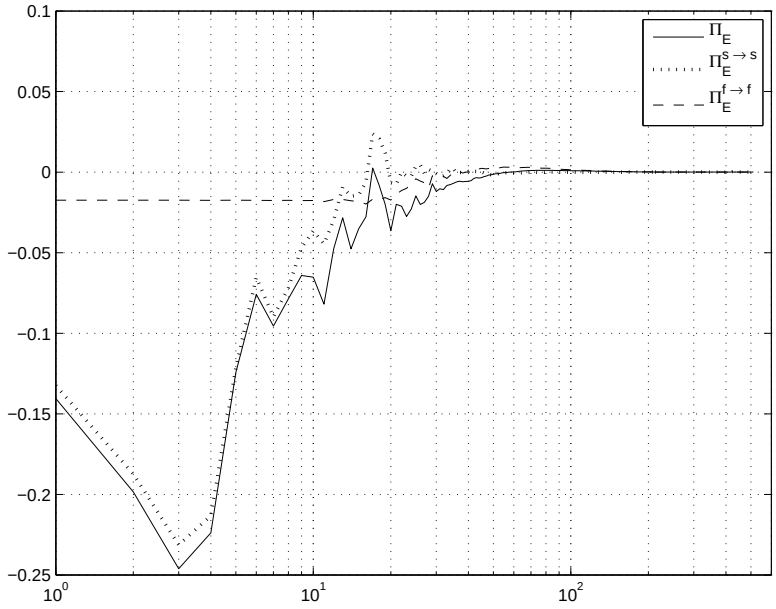

FIGURE 12. Energy fluxes of the whole flow and of the separate structures ($k_{inj} \approx 40$).

Finally, the shifting of the injection scale from $k_{inj} \approx 9$ to $k \approx 40$ essentially influences what is going on before the injection scale but modify only slightly the fluxes beyond it. However, if a much larger injection scale could be set then the enstrophy cascade would be certainly altered. In addition, one can observe that the amplitude of the enstrophy flux increases whith the injection scale. This is due to the fact that the number of vortices also increases with the injection scale.

5. **Decomposition of the transport operator.** We have studied in the previous paragraphs the roles played by the various structures in the global energy and enstrophy transfers and the interactions occurring between them. It is however possible to specify how these interactions take place or more exactly what are the media allowing those transfers. Indeed, thanks to the decomposition of the transport operator itself, it will be shown in this part that the solid rotations of the vortices are the means of transport of the energy and enstrophy transfers.

Thus the transport operator can be decomposed into two parts:

$$(\boldsymbol{v}.\nabla) = (\boldsymbol{v_s}.\nabla) + (\boldsymbol{v_f}.\nabla). \tag{23}$$

By performing this decomposition one can separate the energy or enstrophy transport due to the solid rotations from the transport due to the filaments. Finally each term of the equations (21) and (22) can be also split into two parts leading to the following complete decompositions:

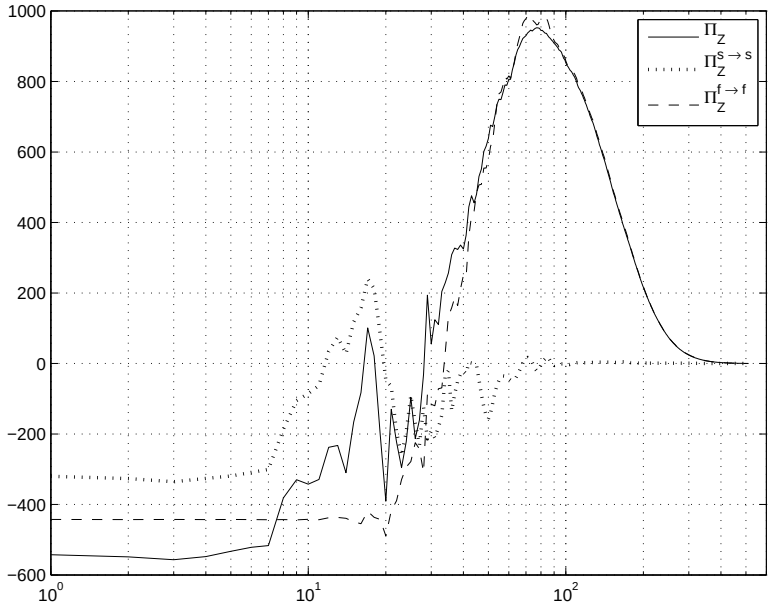

FIGURE 13. Enstrophy fluxes of the whole flow and of the separate structures ($k_{inj} \approx 40$).

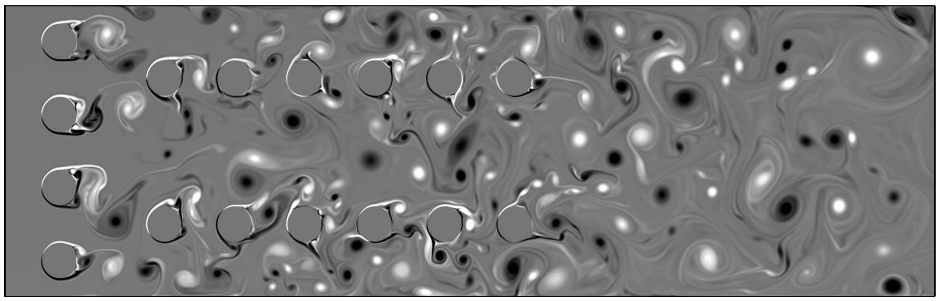

FIGURE 14. Snapshot of the vorticity field

$$
\begin{aligned}
T_E(\boldsymbol{k}) \;=\; & \widehat{\boldsymbol{v_s}^*(\boldsymbol{k})}.\widehat{(\boldsymbol{v_s}.\nabla)\boldsymbol{v_s}}(\boldsymbol{k}) \;+\; \widehat{\boldsymbol{v_s}^*(\boldsymbol{k})}.\widehat{(\boldsymbol{v_f}.\nabla)\boldsymbol{v_s}}(\boldsymbol{k}) \\
& + \widehat{\boldsymbol{v_s}^*(\boldsymbol{k})}.\widehat{(\boldsymbol{v_s}.\nabla)\boldsymbol{v_f}}(\boldsymbol{k}) \;+\; \widehat{\boldsymbol{v_s}^*(\boldsymbol{k})}.\widehat{(\boldsymbol{v_f}.\nabla)\boldsymbol{v_f}}(\boldsymbol{k}) \\
& + \widehat{\boldsymbol{v_f}^*(\boldsymbol{k})}.\widehat{(\boldsymbol{v_s}.\nabla)\boldsymbol{v_s}}(\boldsymbol{k}) \;+\; \widehat{\boldsymbol{v_f}^*(\boldsymbol{k})}.\widehat{(\boldsymbol{v_f}.\nabla)\boldsymbol{v_s}}(\boldsymbol{k}) \\
& + \widehat{\boldsymbol{v_f}^*(\boldsymbol{k})}.\widehat{(\boldsymbol{v_s}.\nabla)\boldsymbol{v_f}}(\boldsymbol{k}). \;+\; \widehat{\boldsymbol{v_f}^*(\boldsymbol{k})}.\widehat{(\boldsymbol{v_f}.\nabla)\boldsymbol{v_f}}(\boldsymbol{k}),
\end{aligned}
\tag{24}
$$

and

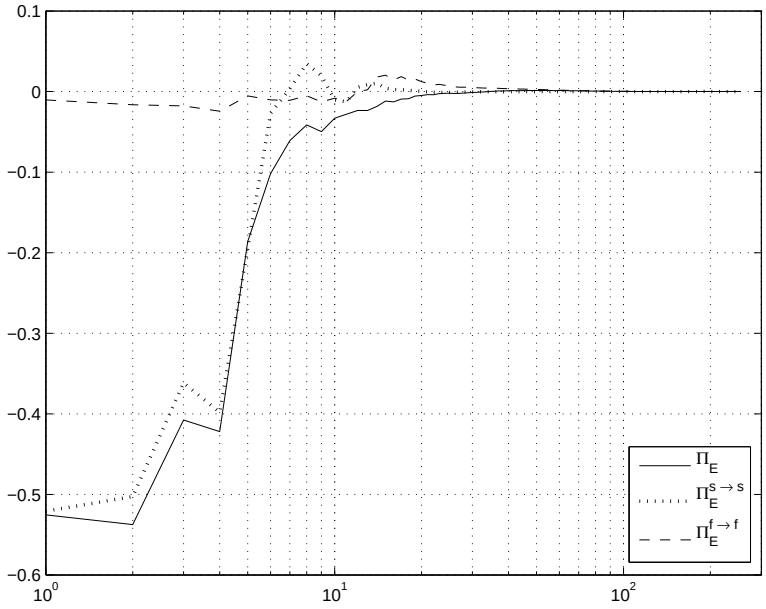

FIGURE 15. Energy fluxes of the whole flow and of the separate structures ($k_{inj} \approx 9$).

$$
\begin{aligned}
T_Z(\boldsymbol{k}) \;=\; & \widehat{\omega_s^*(\boldsymbol{k})}.\widehat{(\boldsymbol{v_s}.\nabla)\omega_s}(\boldsymbol{k}) \;+\; \widehat{\omega_s^*(\boldsymbol{k})}.\widehat{(\boldsymbol{v_f}.\nabla)\omega_s}(\boldsymbol{k}) \\
& + \widehat{\omega_s^*(\boldsymbol{k})}.\widehat{(\boldsymbol{v_s}.\nabla)\omega_f}(\boldsymbol{k}) \;+\; \widehat{\omega_s^*(\boldsymbol{k})}.\widehat{(\boldsymbol{v_f}.\nabla)\omega_f}(\boldsymbol{k}) \\
& + \widehat{\omega_f^*(\boldsymbol{k})}.\widehat{(\boldsymbol{v_s}.\nabla)\omega_s}(\boldsymbol{k}) \;+\; \widehat{\omega_f^*(\boldsymbol{k})}.\widehat{(\boldsymbol{v_f}.\nabla)\omega_s}(\boldsymbol{k}) \\
& + \widehat{\omega_f^*(\boldsymbol{k})}.\widehat{(\boldsymbol{v_s}.\nabla)\omega_f}(\boldsymbol{k}) \;+\; \widehat{\omega_f^*(\boldsymbol{k})}.\widehat{(\boldsymbol{v_f}.\nabla)\omega_f}(\boldsymbol{k}).
\end{aligned}
\tag{25}
$$

For instance, the second term in the right hand side of (25) describes the enstrophy transfer from the solid rotations to themselves by the filamentary structures. One can thus detail the main terms responsible for the fluxes:

$$\Pi_E^{s\to s} = \Pi_E^{s\to s\to s} + \Pi_E^{s\to f\to s}, \tag{26}$$

for the energy transfer and,

$$\Pi_Z^{f\to f} = \Pi_Z^{f\to s\to f} + \Pi_Z^{f\to f\to f}, \tag{27}$$

for the enstrophy transfer. The various terms corresponding to these decompositions have been computed for the first numerical experiment with the injection scale k_{inj} equal to 20 described in the beginning of the paper. The decompositions are given in Figures 17 and 18. The outstanding result of these decompositions is that in both cases the solid rotations are the media responsible for the two transfers. Thus the vortices transport the energy from vortices to vortices and the enstrophy

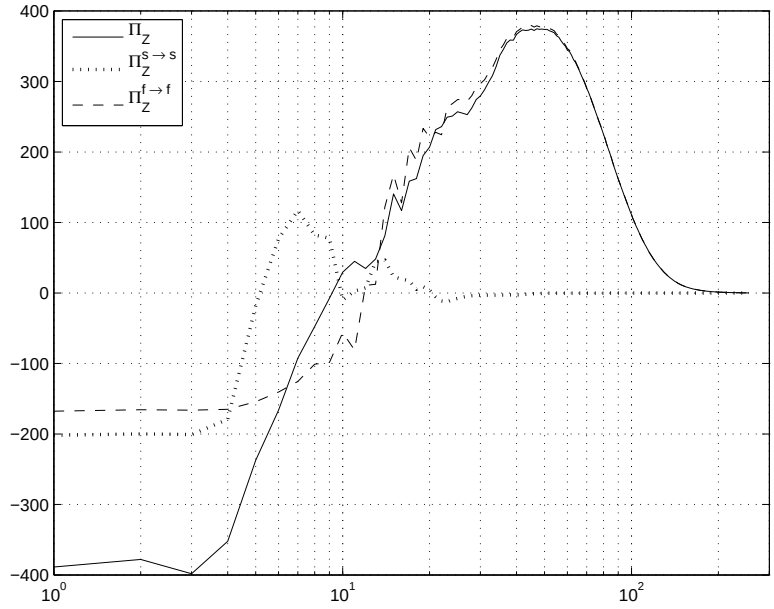

FIGURE 16. Enstrophy fluxes of the whole flow and of the separate structures ($k_{inj} \approx 9$).

from filaments to filaments. The filamentary structures are responsible for the direct enstrophy cascades thanks to the solid rotations dynamics. On the other hand, the inverse energy cascade is completely due to the vortices.

6. **Conclusion.** All the results presented in this paper were obtained with a forcing naturally created by the obstacles. No artificial force has been introduced and the dissipation is only due to the classical term without any hyper or hypo viscosity. The boundary conditions are quite realistic and close to the conditions that can be found in a river with a two dimensional turbulence created by the pillars of a bridge for instance. The theory for this realistic setup does not yet exist, and the comparison to the classical Kolmogorov-Leith-Kraichnan can be only limited. Tran in [15] studied the case of a large-scale transverse flows of incompressible fluid in an elongated doubly periodic domain. He concluded that many questions are still open and should be adressed by numerical methods. Our numerical experiments shed light on this particular problem.
Concerning our specific numerical experiments, we can conclude that an inverse energy cascade and a direct enstrophy cascade exist. An inverse enstrophy cascade and a small direct energy cascade also exist. The importance of these cascades is linked to the size of the injection scale. Furthermore, the energy spectra do not present the classical $k^{-5/3}$ and k^{-3} slopes. We found a scaling law in k^{-2} for the inverse energy transfer and in $k^{-5.5}$ for the enstrophy transfer. The energy cascade is due to an energy transfer inside the core of the vortices and the enstrophy cascade

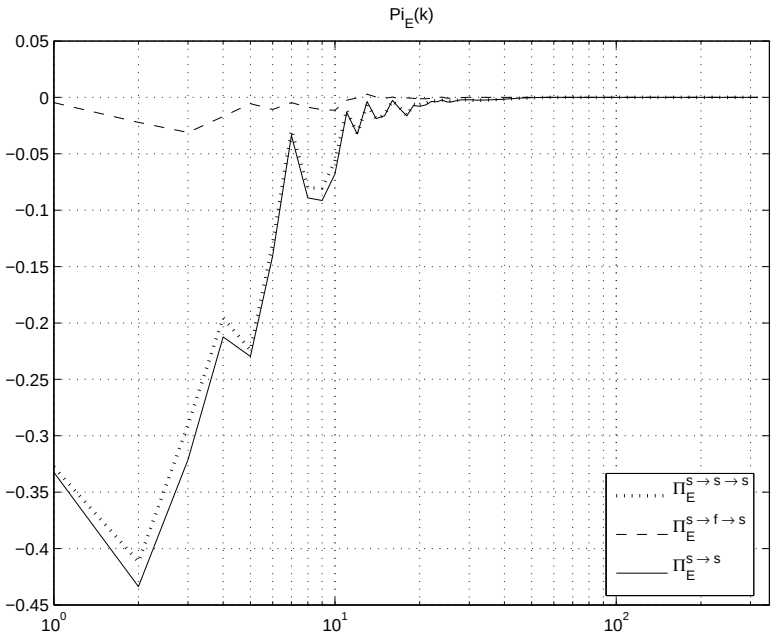

FIGURE 17. Decomposition of the main term responsible for the energy cascade ($k_{inj} \approx 20$).

is due to an enstrophy transfer from filaments to themselves. The structures alowing the two transfers are the solid rotation parts of the vortices.

REFERENCES

[1] Borue V. Inverse energy cascade in stationary two-dimensional homogeneous turbulence Phys. Rev. Lett., 72, 1475-1478, 1994.

[2] Bruneau Ch. H., Fischer P., Peter Z., Yger A. Comparison of Numerical Methods for the Computation of Energy Spectra in 2D Turbulence. Part I: Direct methods Sampl. Theory Signal Image Process. 4, 169-192, 2005.

[3] Bruneau Ch. H., Fischer P., Peter Z., Yger A. Comparison of Numerical Methods for the Computation of Energy Spectra in 2D Turbulence. Part II: Adaptative Algorithms Sampl. Theory Signal Image Process. 4, 271-280, 2005.

[4] Bruneau Ch. H., Fischer P., Kellay H. The structures responsible for the two cascades in two dimensional turbulence Submitted to Phys. Rev. Lett.

[5] Bruneau Ch-H., Kellay H. Coexistence of two inertial ranges in two-dimensional turbulence Phys. Rev. E 71, 046305, 2005.

[6] Fischer P. Multiresolution analysis for two-dimensional turbulence. Part 1: Wavelets vs Cosine packets, a comparative stud Discrete and Continuous Dynamical Systems B 5, 659-686, 2005.

[7] Fischer P., Bruneau Ch.-H. Spectra and filtering: a clarification Submitted to J. Fluid Mech.

[8] Frisch U. Turbulence: The legacy of A. N. Kolmogorov, Cambridge University Press, Cambridge, 1995.

[9] Gkioulekas E., Tung K.K. On the Double Cascades of Energy and Enstrophy in Two Dimensional Turbulence. Part 1. Theoretical Formulation Discrete and Continuous Dynamical Systems B 5, 79-102, 2005.

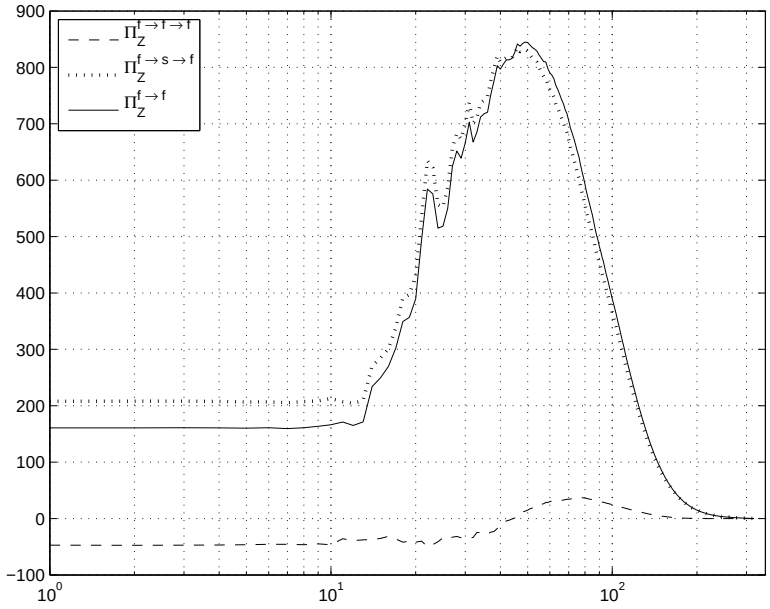

FIGURE 18. Decomposition of the main term responsible for the enstrophy cascade ($k_{inj} \approx 20$).

[10] Gkioulekas E., Tung K.K. On the Double Cascades of Energy and Enstrophy in Two Dimensional Turbulence. Part 2. Approach to the KLB Limit and Interpretation of Experimental Evidence Discrete and Continous Dynamical Systems B, 5, 103-124, 2005.

[11] Kellay H., Goldburg W. I. Two-dimensional turbulence: a review of some recent experiments, Rep. Prog. Phys. 65, 845, 2002.

[12] Obukhov A. M. On the distribution of energy in the spectrum of turbulent flow Dokl. Akad. Nauk SSSR 32, 22-24, 1941.

[13] Obukhov A. M. Spectral energy disctribution in a turbulent flow Izv. Akad. Nauk SSSR Ser. Geogr. Geofiz. 5, 453-466, 1941.

[14] Tabeling P. Two-dimensional turbulence: a physicist approach Phys. Rep. 362, 1-62, 2002.

[15] Tran C. V. Large-scale transverse flows of incompressible fluid in an elongated doubly periodic domain, submitted to J. Fluid Mech.

[16] Tung K.K., Gkioulekas Does the subdominant part of the energy spectrum due to downscale energy cascade remain hidden in quasi-geostrophic turbulence?, submitted to J. Atmos. Sci.

[17] Vassilicos J. C., Hunt J. C. Fractal dimensions and spectra of interfaces with application to turbulence Proc. R. Soc. Lond. A 435, 505-534.

E-mail address: Patrick.Fischer@math.u-bordeaux.fr